

Dynamic cytoplasmic fluidity during morphogenesis in a human fungal pathogen

A. Serrano^{1,2}, C. Puermer^{1,3}, E. Plumb¹, L. Chevalier¹, J. Elferich^{4,5}, L.R. Sinn⁶, N. Grigorieff^{4,5}, M. Ralser⁶, M. Delarue⁷, M. Bassilana¹ & R.A. Arkowitz^{1*}

¹Université Côte d'Azur, CNRS, INSERM, Institute of Biology Valrose (iBV), Nice, France

²Present address: Centro de Biotecnología y Genómica de Plantas, Universidad Politécnica de Madrid (UPM) – Instituto Nacional de Investigación y Tecnología Agraria y Alimentaria (INIA/CSIC), Pozuelo de Alarcón, Spain

³Present address: Department of Microbiology and Immunology, Geisel School of Medicine at Dartmouth, Hanover, NH, USA

⁴RNA Therapeutics Institute, University of Massachusetts Chan Medical School, Worcester, MA, USA

⁵Howard Hughes Medical Institute, University of Massachusetts Chan Medical School, Worcester, MA USA

⁶Charité Universitätsmedizin Berlin, Department of Biochemistry, Berlin, Germany

⁷LAAS-CNRS, University of Toulouse, CNRS, Toulouse, France

*To whom correspondence should be sent: Robert.Arkowitz@univ-cotedazur.fr

Abstract

The molecular crowding of the cytoplasm impacts a range of cellular processes. Using a fluorescent microrheological probe (GEMs), we observed a striking decrease in molecular crowding during the yeast to filamentous growth transition in the human fungal pathogen *Candida albicans*. This decrease in crowding is due to a decrease in ribosome concentration that results in part from an inhibition of ribosome biogenesis, combined with an increase in cytoplasmic volume; leading to a dilution of the major cytoplasmic crowder. Moreover, our results suggest that inhibition of ribosome biogenesis is a trigger for *C. albicans* morphogenesis.

The cytoplasm is a crowded environment and molecular crowding can affect a range of biological functions^{1,2}, including chemical reaction rates, protein complex formation and rates of cytoskeletal protein polymerization³⁻⁵. In the budding yeast *Saccharomyces cerevisiae* and mammalian cells the target of rapamycin complex (TORC) was shown to regulate ribosome concentration, and inhibition of TORC1 resulted in increased cytoplasmic fluidity⁶. More recently, cell cycle arrest mutants were shown to result in decreased macromolecular crowding of the cytoplasm, in part *via* ribosome downregulation⁷. Little is known about the relationship between molecular crowding in the cytoplasm and morphological growth states, for example when the human fungal pathogen *Candida albicans* switches from an ovoid yeast form to a filamentous hyphal form, a transition essential for virulence. Here, we show that there is a dramatic decrease in molecular crowding during filamentous growth, which is mediated by inhibition of ribosome biogenesis and subsequent dilution of this critical cytoplasmic crowder as a result of new growth. We propose that ribosome levels are tuned to regulate crowding in distinct growth states in this fungal pathogen. Furthermore, our results highlight that despite the new growth that occurs during the yeast-to hyphal transition, there is a substantial decrease in ribosome levels.

To investigate the link between cytoplasmic diffusivity at the mesoscale and cell morphology we took advantage of passive microrheological probes⁶, for which we can measure dynamics both in budding and hyphal cells. We used *C. albicans* cells expressing 40-nm GEMs. We imaged every 30 msec to obtain a signal sufficient for single particle tracking. The mean track length was 10 frames, which corresponds to 300 msec of imaging. The effective diffusion coefficient, D_{eff} , which is inversely proportional to microviscosity for Brownian motion, was determined from the first 120 msec of acquisition. Temporal projections that were false colored for GEM distribution in budding cells, fixed budding cells and cells treated with fetal bovine serum for 60 min, in which a filament is evident, are shown in Figure 1A, with trajectories of GEMs in representative budding and filamentous cells. Fixation

55 reduced the GEM D_{eff} of cells by over 10-fold. The median effective coefficient of diffusion in budding
56 cells was $\sim 0.1 \mu\text{m}^2 \text{s}^{-1}$ (Fig. 1B). This value was independent of GEM expression level, with similar
57 D_{eff} observed with *TEF1* and *ADHI* promoter driven expression (Fig. S2), and somewhat lower than
58 that observed in *S. cerevisiae*⁶.

59
60 After 1-2 hr incubation in serum, filaments formed with an average length of 12 μm (range of 2 – 22
61 μm). We observed a striking increase in GEM D_{eff} of ~ 2 -fold in these filamentous cells, which
62 corresponds to a substantial fluidization of the cytoplasm (Fig. 1B, S3). We speculated that some of the
63 GEM D_{eff} variation in filamentous cells could be due to the different filament lengths. Hence, we
64 examined whether cytoplasmic diffusivity scaled with filament length, which is directly proportional to
65 cell volume. Figure 1C shows a correlation between filament length and cytoplasmic diffusivity; when
66 values were grouped in 2 μm filament length bins we observe a strong positive correlation between D_{eff}
67 and filament length, with a Pearson coefficient of 0.93. The median D_{eff} in the mother and filament
68 compartments was examined and there was a small, but significant decrease in the filament, compared
69 to mother compartment and whole cell (Fig. S4A). This is consistent with changes in the surface to
70 volume, as shown in our diffusion simulations (Fig. S5, compare red-sphere to blue-cylinder bars).

71
72 Cytoplasmic fluidization scaling with increased cell volume suggests that during hyphal morphogenesis
73 there is substantial dilution of a molecular crowder, such as ribosomes. To test this hypothesis, we
74 simulated the diffusion of mesoscale particles in spherical and cylindrical cell geometries, with an
75 equivalent initial crowder/cell volume of 14,000 ribosomes/ μm^3 cytoplasm, based on values from *S.*
76 *cerevisiae*, which accounts for 20% of the initial cytoplasmic volume⁶. We also investigated the effect
77 of the addition of large intracellular excluded volumes (analogous to vacuoles in volume) on the
78 simulation of ribosome D_{eff} (Fig. S5). As expected, we found that in contrast to the small effects of cell
79 geometry, the addition of inaccessible space dramatically reduced D_{eff} (between 50-70%, depending on
80 geometry). Note that the increase in cell volume during morphogenesis is greater than that from solely
81 cell geometry changes, as the vacuole, which is GEM inaccessible, is localized predominantly to the
82 mother cell portion (Fig. S1B)^{9,10}. Therefore, we simulated the effect of doubling the cell volume, which
83 occurs approximately every hour with filament elongation, maintaining the amount of cytoplasmic
84 crowder. Figure 1D shows that, in such a simulation (irrespective of geometry), we also observe a
85 significant increase in D_{eff} (~ 2 -fold), similar to the experimental data (Fig. 1C). These results are
86 consistent with a striking dilution of a cytoplasmic crowder - on the order of 4-5-fold - due to both
87 increased overall cell volume and accessible volume in the filament, as a result of less vacuoles (Fig
88 S6). These simulations reveal that the decreased crowding could be due to a combination of a decrease
89 in ribosome biogenesis, and an increase in accessible volume, both of which decrease crowding.

90
91 Hence, we tested this theoretically using the simplified formalism that describes diffusion with respect
92 to energy transfer in polydispersed mixtures (*eq 2*)⁸ to fit our data and derive the ribosome concentration,
93 assuming they were the main crowding agent. We assumed that during filament growth, ribosomes are
94 only diluted (*i.e.* no new synthesis). Fitting the experimental data using this equation allowed us to
95 extract the initial concentration of ribosomes in the mother cell compartment, *i.e.* $24,000 \pm 300$
96 ribosomes/ μm^3 of cytoplasmic volume (Fig. 1C, predicted). In addition, when we took into account the
97 fraction of GEM accessible volume (Fig. S6), in *eq 2*, we still observed a good fit to the experimental
98 data, yielding a ribosome concentration (c_{ribo}) of $20,000 \pm 700/\mu\text{m}^3$ (Fig. S7), which is somewhat higher
99 than that determined in *S. cerevisiae*⁶. The lower D_{eff} in *C. albicans* suggests that budding cells are more
100 crowded in this fungal pathogen compared to *S. cerevisiae*.

101
102 As ribosomes are likely to be the predominant cytoplasmic crowder, we used liquid-chromatography
103 tandem mass spectrometry (LC-MS/MS) to determine the relative abundance of ribosomal proteins,
104 which decreased upon filamentation, compared to budding cells (Fig. S8). This is in agreement with the
105 decreased (~ 2 -fold) levels of ribosomal RNA reported in *C. albicans* filamentous cells¹¹, as well as a
106 substantial decrease in the transcripts of many ribosomal proteins upon filamentation¹². To directly
107 assess ribosome levels during morphogenesis we carried out cryogenic electron microscopy (cryo-EM)
108 coupled with 2D template-matching (2DTM) to identify 60S ribosomes^{13,14} (Figure S9, S10). Figure 1E

109 shows that in filamentous cells there is a marked decrease in ribosome concentration, which is filament
110 length dependent (Fig. 1F). Together, our results reveal that changes in crowding at the mesoscale
111 occurs, in part, *via* ribosomes, although we cannot exclude the possibility that there is also a decrease
112 in the concentration of larger, slowly diffusing polysomes¹⁵ and/or changes in cytoplasmic viscosity.
113 The increased GEM D_{eff} in the filamentous cells could also be the result of decreased turgor pressure,
114 hence we examined how mesoscale cytoplasmic diffusivity was affected by changes in external
115 osmolarity using sorbitol. At all sorbitol concentrations examined we observed an increased GEM D_{eff}
116 in filamentous compared to budding cells (Fig. 2A). Furthermore, a higher concentration of sorbitol is
117 required to fully abolish GEM movement in filamentous cells, suggesting that molecular crowding in
118 such cells is reduced (Fig. S11A, B).

119
120 We also examined whether mesoscale cytoplasmic diffusivity was affected by depolymerization of the
121 actin cytoskeleton, as it was shown to decrease cytoplasmic diffusivity in *S. cerevisiae*⁶, yet had no
122 effect in *S. pombe*¹⁶. Figures 2B and S12 show that in budding *C. albicans* cells the GEM D_{eff} increased
123 ~35% upon Latrunculin A (LatA) disruption of F-actin. In contrast, the same treatment had a
124 substantially smaller effect on the GEM cytoplasmic dynamics in filamentous cells (Fig. 2C and S12).
125 However, in LatA treated filamentous cells there was no longer a difference between the GEM D_{eff} in
126 the filament compartment and that of the whole cell (Fig. S4B), indicating that the actin cytoskeleton,
127 rather than solely cell geometry, is important for the small difference in the cylindrical filament (Fig.
128 S5). Overall, these results indicate that actin is more critical for cytoplasmic crowding in budding cells
129 compared to hyphal cells, in part due to the decreased accessible cytoplasm volume in budding cells
130 (Fig. S6). As LatA also blocks growth, these results also reveal that growth *per se* does not substantially
131 contribute to cytoplasmic mesoscale crowding in filamentous cells. This is further confirmed in Figure
132 2D, which shows that over a 2-fold range of filament extension rates, GEM D_{eff} was essentially constant.

133
134 The increase in cytoplasmic fluidity, as a result of the decreased ribosome concentration upon filament
135 elongation, suggested that inhibition of ribosome biogenesis may be important for filamentous growth.
136 This would lead to dilution of ribosome crowdens upon subsequent growth. To investigate the role of
137 ribosome biogenesis in morphogenesis, we generated a mutant defective in the former process. *CGR1*
138 encodes a protein that is critical for the processing of pre-rRNA in *S. cerevisiae*¹⁷, in particular rRNA
139 for the 60S ribosome subunit. Addition of doxycycline (Dox) to a *C. albicans* strain in which the sole
140 copy of *CGR1* is under the control of the Tet-repressible promoter, resulted in complete repression of
141 *CGR1* mRNA transcript (Fig. S13A) and in slow growth (Fig. S13B). Analyses of rRNA levels revealed
142 a decrease in 28S and 18S rRNA upon *CGR1* repression (Fig. S13C) and a substantial (~1.7-fold)
143 increase in GEM D_{eff} (Fig 2E). Strikingly, repression of *CGR1* resulted in some filamentous cells in the
144 absence of serum, which was not observed in the absence of Dox nor in wild-type cells (Fig. 2F).
145 Furthermore, Figure 2G shows a dramatic induction of the hyphal specific genes *e.g.* those encoding
146 the G1 cyclin, *HGCI*, the candidalysin toxin, *ECE1*, and the hyphal cell wall glycoprotein, *HWPI*, in
147 the *cgr1* mutant in the presence of Dox. Similarly, inhibition of the Tor kinase by rapamycin, which has
148 been shown to reduce the number of ribosomes in *S. cerevisiae*, resulted in hyphal specific gene
149 induction in *C. albicans*¹⁸. Together these results reveal that inhibition of ribosomal biogenesis is
150 important for the yeast to hyphal morphogenetic transition and that, upon filament elongation, dilution
151 of ribosomes leads to a substantial reduction in cytoplasmic crowding.

152
153 In *S. cerevisiae*, a sizeable portion of ribosomes (at least 25%) do not contribute to translation¹⁹.
154 Intriguingly, while *C. albicans* filamentous growth (0.3 $\mu\text{m}/\text{min}$ extension) is similar with respect to
155 volume increase, when compared to budding growth (doubling every 90 min), genome dilution upon
156 DNA replication arrest in *E. coli* was reported to result in a decrease in active ribosomes and sub-
157 optimal growth²⁰. Increased cytoplasmic fluidity has been shown to increase cytoskeleton
158 polymerization and depolymerization rates in fission yeast⁵, suggesting that decreased molecular
159 crowding at the mesoscale could also be beneficial for *C. albicans* filamentous growth. In summary,
160 our results reveal a striking change in cytoplasmic molecular crowding during morphogenesis (Fig.
161 2H), which is critical for the virulence of this human fungal pathogen, as a result of dilution of
162 ribosomes subsequent to inhibition of their biogenesis. Our results suggest that changes in cytoplasmic

163 diffusion at the mesoscale, by tuning ribosome numbers, are intimately associated with filamentous
164 growth.

165 **References**

- 166
- 167 1 Holt, L. J. & Delarue, M. Macromolecular crowding: Sensing without a sensor. *Curr Opin Cell*
- 168 *Biol* **85**, 102269 (2023). <https://doi.org/10.1016/j.ceb.2023.102269>
- 169 2 Subramanya, A. R. & Boyd-Shiwarski, C. R. Molecular Crowding: Physiologic Sensing and
- 170 Control. *Annu Rev Physiol* **86**, 429-452 (2024). [https://doi.org/10.1146/annurev-physiol-](https://doi.org/10.1146/annurev-physiol-042222-025920)
- 171 [042222-025920](https://doi.org/10.1146/annurev-physiol-042222-025920)
- 172 3 Demosthene, B., Lee, M., Marracino, R. R., Heidings, J. B. & Kang, E. H. Molecular Basis for
- 173 Actin Polymerization Kinetics Modulated by Solution Crowding. *Biomolecules* **13** (2023).
- 174 <https://doi.org/10.3390/biom13050786>
- 175 4 Miermont, A. *et al.* Severe osmotic compression triggers a slowdown of intracellular signaling,
- 176 which can be explained by molecular crowding. *Proc Natl Acad Sci U S A* **110**, 5725-5730 (2013).
- 177 <https://doi.org/10.1073/pnas.1215367110>
- 178 5 Molines, A. T. *et al.* Physical properties of the cytoplasm modulate the rates of microtubule
- 179 polymerization and depolymerization. *Dev Cell* **57**, 466-479 e466 (2022).
- 180 <https://doi.org/10.1016/j.devcel.2022.02.001>
- 181 6 Delarue, M. *et al.* mTORC1 Controls Phase Separation and the Biophysical Properties of the
- 182 Cytoplasm by Tuning Crowding. *Cell* **174**, 338-349 e320 (2018).
- 183 <https://doi.org/10.1016/j.cell.2018.05.042>
- 184 7 Terhorst, A. *et al.* The environmental stress response regulates ribosome content in cell cycle-
- 185 arrested *S. cerevisiae*. *Front Cell Dev Biol* **11**, 1118766 (2023).
- 186 <https://doi.org/10.3389/fcell.2023.1118766>
- 187 8 Ilker, E., Castellana, M. & Joanny, J. F. Long-time diffusion and energy transfer in polydisperse
- 188 mixtures of particles with different temperatures. *Phys Rev Res* **3** (2021).
- 189 <https://doi.org/10.1103/PhysRevResearch.3.023207>
- 190 9 Veses, V. & Gow, N. A. Vacuolar dynamics during the morphogenetic transition in *Candida*
- 191 *albicans*. *FEMS Yeast Res* **8**, 1339-1348 (2008). [https://doi.org/10.1111/j.1567-](https://doi.org/10.1111/j.1567-1364.2008.00447.x)
- 192 [1364.2008.00447.x](https://doi.org/10.1111/j.1567-1364.2008.00447.x)
- 193 10 Veses, V., Richards, A. & Gow, N. A. Vacuoles and fungal biology. *Curr Opin Microbiol* **11**,
- 194 503-510 (2008). <https://doi.org/10.1016/j.mib.2008.09.017>
- 195 11 Fleischmann, J. & Rocha, M. A. Decrease in Ribosomal RNA in *Candida albicans* Induced by
- 196 Serum Exposure. *PLoS One* **10**, e0124430 (2015).
- 197 <https://doi.org/10.1371/journal.pone.0124430>
- 198 12 Nantel, A. *et al.* Transcription profiling of *Candida albicans* cells undergoing the yeast-to-
- 199 hyphal transition. *Mol Biol Cell* **13**, 3452-3465 (2002). [https://doi.org/10.1091/mbc.e02-05-](https://doi.org/10.1091/mbc.e02-05-0272)
- 200 [0272](https://doi.org/10.1091/mbc.e02-05-0272)
- 201 13 Lucas, B. A. *et al.* Locating macromolecular assemblies in cells by 2D template matching with
- 202 cisTEM. *Elife* **10** (2021). <https://doi.org/10.7554/eLife.68946>
- 203 14 Lucas, B. A., Zhang, K., Loerch, S. & Grigorieff, N. In situ single particle classification reveals
- 204 distinct 60S maturation intermediates in cells. *Elife* **11** (2022).
- 205 <https://doi.org/10.7554/eLife.79272>
- 206 15 Mohapatra, S. & Weisshaar, J. C. Functional mapping of the E. coli translational machinery
- 207 using single-molecule tracking. *Mol Microbiol* **110**, 262-282 (2018).
- 208 <https://doi.org/10.1111/mmi.14103>
- 209 16 Garner, R. M., Molines, A. T., Theriot, J. A. & Chang, F. Vast heterogeneity in cytoplasmic
- 210 diffusion rates revealed by nanorheology and Doppelganger simulations. *Biophys J* **122**, 767-
- 211 783 (2023). <https://doi.org/10.1016/j.bpj.2023.01.040>
- 212 17 Moy, T. I., Boettner, D., Rhodes, J. C., Silver, P. A. & Askew, D. S. Identification of a role for
- 213 *Saccharomyces cerevisiae* Cgr1p in pre-rRNA processing and 60S ribosome subunit synthesis.
- 214 *Microbiology (Reading)* **148**, 1081-1090 (2002). [https://doi.org/10.1099/00221287-148-4-](https://doi.org/10.1099/00221287-148-4-1081)
- 215 [1081](https://doi.org/10.1099/00221287-148-4-1081)
- 216 18 Bastidas, R. J., Heitman, J. & Cardenas, M. E. The protein kinase Tor1 regulates adhesin gene
- 217 expression in *Candida albicans*. *PLoS Pathog* **5**, e1000294 (2009).
- 218 <https://doi.org/10.1371/journal.ppat.1000294>

219 19 Metzl-Raz, E. *et al.* Principles of cellular resource allocation revealed by condition-dependent
220 proteome profiling. *Elife* **6** (2017). [https://doi.org:10.7554/eLife.28034](https://doi.org/10.7554/eLife.28034)
221 20 Mäkelä, J. *et al.* Genome concentration limits cell growth and modulates proteome composition
222 in *Escherichia coli*. *Elife* (2024).
223
224

225 MATERIAL AND METHODS

226

227 Strains and media

228 Strains used in this study are listed in Table S1. For transformation, strains were grown in YEPD (yeast
229 extract, peptone, dextrose) supplemented with Uridine (80 $\mu\text{g/ml}$) at 30°C. Cells were grown in YEPD
230 medium, supplemented with Uridine at 30°C for budding growth. For filament induction cells, cells
231 were either grown in YEPD liquid media with 50% fetal bovine serum (FBS; PAN Biotech) or on
232 agarose pads with 75% FBS in synthetic complete (SC) media, both at 37°C. In all experiments that
233 involved comparison with filamentous cells, budding cells were briefly incubated in the same media at
234 37°C prior to imaging at the same temperature. For doxycycline (Dox) gene repression, YEPD was
235 supplemented with 5 $\mu\text{g/ml}$ Dox. For sorbitol experiments, budding and filamentous cells were
236 incubated with the indicated final concentrations of sorbitol for 5 min prior to imaging at 37°C. For
237 Latrunculin A (LatA) actin depolymerization, cells were incubated with either 200 or 400 μM LatA, for
238 budding and filamentous cells, respectively, during 15 min prior to imaging.

239

240 The oligonucleotides used in this study are listed in Table S2. The PfV gene, which encodes the subunits
241 that comprise a 40-nm genetically encoded multimeric (GEM) nanoparticle¹ was codon optimized for
242 *C. albicans* and synthesized (BaseClear, Netherlands). The CaPfV gene was cloned from the pUC57
243 vector into the pFA-GFP γ -URA3 plasmid using PstI sites, resulting in the pFA-CaPfV-GFP γ -URA3
244 plasmid. The *URA3* marker was replaced with either *CdHIS1* and *ARG4* markers, using unique AscI
245 and PmeI restriction sites, resulting in pFA-CaPfV-GFP γ -CdHIS1 and pFA-CaPfV-GFP γ -ARG4. The
246 GFP γ was then mutated using site directed mutagenesis to a monomeric version using primers
247 CaGFP γ pA206K-BamHI/CaGFP γ mA206K-BamHI, yielding pFA-CaPfV-GFP γ ^{A206K}-CdHIS1 and
248 pFA-CaPfV-GFP γ ^{A206K}-ARG4. Subsequently these two plasmids were used as a template to PCR
249 amplify the CaPfV-GFP γ ^{A206K}-CdHIS1 and pFA-CaPfV-GFP γ ^{A206K}-ARG4 cassettes for integration
250 behind the endogenous *ADH1* promoter by using primers ADH1p-PfVp and CaADH1KixFP_S2. The
251 tetracycline repressible *cgr1* Δ /pTet*CGR1* strain was constructed from PY173, a derivative of BWP17
252 containing the tetracycline-regulatable transactivator TetR-SchAP4AD, as described². To visualize F-
253 actin, a LifeAct reporter was used which was derived from the plasmid pYGS974 (TEF1 Δ LifeAct-GFP-
254 HIS1/pJET)³, in which GFP was replaced by mScarlet using primers NotI Tef1pLifeActS1 and
255 CamScarletmAscI, resulting in pTEF1p-LifeAct-mScarlet-HIS1. This plasmid was digested with
256 NotI/XbaI and integrated by homologous recombination in the *TEF1* locus.

257

258 Microscopy, sample preparation and image analysis.

259 **Light microscopy.** The GEM nanoparticles were imaged, using TIRF on a Nikon Ti eclipse inverted
260 microscope (Nikon France S.A.S., Champigny-sur-Marne, France) equipped with an iLas² scan head
261 (Roper scientific, Evry, France), an iXon 888 EMCCD camera (Andor technology, Belfast, UK) and a
262 100x CFI-APO-TIRF oil NA 1.49 objective. The laser illumination was with a 488 nm diode laser, with
263 an intensity ranging between 10-60% and a TIRF angle of 56.24°. Images were acquired as a stream of
264 300-600 images in a single Z plane, with a 30 msec image acquisition and readout time, unless otherwise
265 indicated. Temperature was controlled with an Okolab incubator (Ottaviano, Italy) at 37°C, unless
266 otherwise indicated. The LifeAct reporter was imaged using the spinning-disk confocal modality on the
267 above described microscope, equipped with a Yokogawa CSU-W1 (Yokogawa Electric Corporation,
268 Tokyo, Japan), and using a 561 nm diode laser. Multi-positions were acquired with a motorized XYZ
269 stage. The effective diffusion of the GEM particles was calculated as described¹, using the plugin
270 Mosaic⁴ in Fiji (version 1.54f) in a Windows 10/Intel computer and Matlab (version R2023a). Matlab
271 was also used to generate the plots of all trajectories using a colormap, and to split the filamentous cells
272 in order to analyze mother cell vs filament effective diffusion (scripts available upon request). Extension
273 rates were calculated as a function of filament length (measured with Fiji) per time. Scale bar is 5 μm .

274

275 **Electron microscopy.** Cryoplunging was carried out essentially as described⁵. Au grids (200 mesh)
276 with a 2/2 silicone oxide support film were glow-discharged on both sides for 45 sec at 20 mA. Glycerol
277 (5% final concentration) was added to cells and then immediately 3 μl (0.2 OD₆₀₀) cell suspension was
278 applied to the support film side of grids, blotted for 10 sec and then frozen in liquid ethane using a

279 cryoplunger (GP2 Leica, Wetzlar, Germany) and frozen. FIB-milling was carried out using an Aquilos
280 2 FIB/SEM (Thermo Fisher, Waltham, MA) with a stage cooled to $< -190^{\circ}\text{C}$ in a 35° AutoGrid sample
281 holder. Grids were sputter-coated with metallic Pt and then coated with organo-Pt essentially as
282 described⁵. An overview of the grid was created by montaging SEM images and isolated cells or cell
283 clusters at the center of grid squares were selected for FIB-milling. Lamellae were generated
284 automatically using the AutoTEM software (Thermo Fisher, Waltham, MA), with the following
285 protocol: rough milling 1: 1 nA; medium milling 2: 0.3 nA (1.0° overtilt); fine milling 0.1 nA (0.5°
286 overtilt); finer milling 0.1 nA (0.5° overtilt); lamella polishing: 50 and 30 pA, 0.2° overtilt resulting in
287 150 nm thick lamellae which were subsequently sputter-coated with Pt for 5 sec at a current of 5mA.

288
289 FIB-milled grids were imaged in a Titan Krios TEM (Thermo Fisher, Waltham, MA) operated at 300
290 keV and equipped with a BioQuantum energy filter (Gatan, Pleasanton, CA) and K3 camera (Gatan,
291 Pleasanton, CA). The instrument was controlled using SerialEM⁶. Individual lamellae were manually
292 centered in the microscope and then moved to a position $60\ \mu\text{m}$ below the eucentric height to achieve
293 fringe-free illumination. The stage was tilted 15° to compensate for the milling angle and overview
294 images were obtained with a pixel size of $76.8\ \text{\AA}$. Individual cells were annotated in these overview
295 images using napari⁷ and high-resolution montages were obtained for these cells using DeCo-LACE
296 acquisition scripts⁸. The physical pixel size in high-resolution exposures was $1.05\ \text{\AA}$, defocus was
297 maintained at $1\ \mu\text{m}$, and the total exposure was $30\ \text{e}/\text{\AA}^2$. The exposures were dose-fractionated into 30
298 frames.

299
300 Movies were imported into the cisTEM software package⁹ and motion-corrected using a custom version
301 of unblur¹⁰ as described⁸, and binned to a final pixel size of $2.0\ \text{\AA}$. CTF parameters and sample thickness
302 were estimated using CTFFIND5¹¹. The structure of the vacant *C. albicans* 80S ribosome¹² (PDB code:
303 7PZY) was modified by deleting subunits corresponding to the 40S subunit and the resulting 60S
304 structure was converted to a density map at $2.0\ \text{\AA}$ pixel size using the simulate program in cisTEM¹³
305 using a B-factor scaling of 2. 2D template matching of individual exposures was performed using the
306 GPU-accelerated version of the match_template program in the cisTEM suite¹⁴. Rotation angles were
307 search using a 2 in-plane and 3 out-of-plane step-size and defocus values were searched with a 240 nm
308 slab at a 40 nm step size. Image data and template matching results were montaged together as
309 described⁸.

310
311 The number of 60S ribosome subunits per imaged area was determined by manually segmenting
312 cytoplasmic areas from the montaged cryo-EM images (Fig. 1F, S9 and S10) and dividing the number
313 of detections within the segmentation by the segmented area. The imaged volume was calculated
314 by fitting the thickness of individual exposures, as estimated by CTFFIND5, to a 2-dimensional cubic
315 B-spline model with 3 knots¹⁹ and integrating the estimated thickness at every pixel of the segmented
316 area. The variation of this measurement was estimated by repeating this calculation in 50 random square
317 areas with a side-length of 200 nm within the segmented area.

318
319 **Modeling cytoplasmic diffusion**

320 **Predictive equations.** A simplified formalism¹⁵ was used to describe diffusion with respect to energy
321 transfer in polydispersed mixtures to determine the fit to our experimental data and from these equations
322 (eq 1 and 2) we derived the number of ribosome crowders:

$$323 \quad D = D_0(1 - a\varphi) ; \quad \varphi = \frac{V_{\text{ribo}}}{V_m + V_f}; \quad a = \frac{(R_{\text{ribo}} + R_{\text{GEMs}})^2}{R_{\text{GEMs}}^2} \quad (1)$$

324
325 With V_i being the volume of the ribosomes (ribo), the mother part of the cell (m) and the filament (f).
326 D_0 is the diffusion coefficient of GEMs in the absence of ribosomes, but with other crowders in the cell.
327 To avoid this unknown, we define \widetilde{D}_0 as the diffusion coefficient of GEMs when there is no filament
328 (about $0.1\ \mu\text{m}^2/\text{s}$ in our case). This results in:

$$329 \quad D = \widetilde{D}_0 \frac{1 - \frac{V_{\text{ribo}} a}{V_m + V_f}}{1 - \frac{V_{\text{ribo}} a}{V_m}} \quad (2)$$

330

331 We used *eq* (2) to fit our data. Since we assume that no more ribosomes are produced during the growth
332 of the filament, the total volume of ribosomes is fixed by the initial condition of the volume of the
333 mother compartment, and is equal to $V_{\text{ribo}} = c_{\text{ribo}} \times v_{\text{ribo}} \times V_m$ where $v_{\text{ribo}} = 4/3\pi R_{\text{ribo}}^3$ is the
334 volume of 1 ribosome, assuming a spherical geometry. The only unknown in *eq* (2) is thus c_{ribo} .
335

336 **Simulations.** A Matlab-based model (version R2023a) was developed to simulate particle diffusion
337 within spherical and cylindrical boundaries, which we refer to as DiffSim. Particles of radii and
338 concentration similar to that of ribosomes ($r = 14 \text{ nm}$ and $11,100/\mu\text{m}^3$) were randomly localized within
339 these geometries, together with larger spherical crowders (similar in size to a vacuole taking up 60% of
340 cell volume) which were immobile. To facilitate computation in this 3D simulation, cell geometries and
341 excluded volumes were chosen accordingly. The model incorporated three primary forces affecting
342 particle diffusion: Brownian motion and collisions with both other particles and crowders. Brownian
343 motion was modeled using a random walk algorithm, where particles were displaced randomly at each
344 time step. Collisions were simulated using a hard-sphere model, deflecting particles upon contact.
345 Similarly, when particles encountered external boundaries, they were deflected back into the system.
346 Particle positions were recorded in a matrix for subsequent analysis. The mean-squared displacement
347 (MSD) was calculated as a function of time (with Δt being identical to GEM acquisitions) to assess the
348 effective diffusion coefficient and its dependence on relative cell geometry and volume was determined.
349 The effective diffusion coefficient (D_{eff}) was then determined from the slope of the MSD curve using
350 the Einstein-Smoluchowski equation. The accessible volume was determined using a custom Matlab
351 program, which we refer to as AccessCyto, which analyzed the positions of GEM particle tracks to
352 calculate the region of the cell that was accessible to particle movement. The accessible volume was
353 then compared to the total cell volume, by segmenting the maximum projections, to calculate the
354 percentage of the cell accessible to the GEM particles. Scripts available upon request.
355

356 **Proteomics**

357 Sample preparation was essentially as described¹⁶. Quality control samples to monitor LC-MS
358 performance were created from pooling small aliquots of all samples. Peptide quantities were estimated
359 *via* Quantitative Fluorometric Peptide Assay (Pierce). LC-MS based proteomic data acquisition was
360 performed as described¹⁷. In brief, samples were injected on a ACQUITY M-Class HPLC (Waters)
361 connected to a ZenoTOF 7600 mass spectrometer with an Optiflow source (SCIEX), separated on a
362 HSS T3 column (300 $\mu\text{m} \times 150 \text{ mm}$, 1.8 μm ; Waters) using a 20 min active gradient. We used a Zeno
363 SWATH acquisition scheme with 85 variable-sized windows and 11 ms accumulation time. LC-MS
364 raw data was processed using DIA-NN 1.8¹⁸. First, a spectral library was predicted including the
365 UniProt Proteome of *C. albicans* SC5314 (<https://www.uniprot.org/proteomes/UP000000559>), as well
366 as the sequence of the genetically encoded multimeric nanoparticle (see description above). For the
367 main search, we enabled tryptic digestion allowing for one missed cleavage, no variable modification,
368 N-terminal Methionine excision and carbamidomethylation as fixed modification of Cysteines. Mass
369 accuracies were set to fall within 20 ppm and match-between-runs was enabled with protein inference
370 on Protein level. The obtained report was processed using Python 3.9 with the pandas (1.4.3), NumPy
371 (1.23.0) and Seaborn (0.11.2) packages. Data was filtered to less or equal than 1% FDR concerning
372 Global.Q.Value, as well as PG.Q.Value and Lib.PG.Q.Value. Prior to plotting, protein group intensities
373 were sample-wise median normalized in two steps: first, subtracting the sample median in log₂-space,
374 then subtracting the log₂-sample median of entities not belonging to the ribosome, according to UniProt
375 annotated protein names (*i.e.* containing “60S” or “40S, that is the 76 core ribosome proteins”).
376

377 **RNA extraction and RT-PCR**

378 Cells were grown in YEPD media in the presence or absence of 5 $\mu\text{g/ml}$ of Dox. RNA extraction and
379 RT-PCR were carried out as described²⁰. Oligonucleotide pairs ACT1.P1/ACT1.P2,
380 CGR1.P1/CGR1.P2, ECE1.P1/ECE1.P2, HGC1.P1/HGC1.P2 and HWP1.P1/HWP1.P2 were used to
381 amplify *ACT1*, *CGR1*, *ECE1*, *HGC1* and *HWP1*, respectively.
382

383 **Statistical analysis**

384 Data were compared by the Mann-Whitney U test and where relevant the paired or unpaired t-test using
385 GraphPad Prism (v. 8) software, with all p values indicated in figure legends. Unless stated otherwise
386 medians and interquartile ranges are indicated. Pearson correlation coefficient and simple linear
387 regression were determined using GraphPad Prism (v. 8) software.

388 **Acknowledgements**

389 We thank P. Silva, H. Labbaoui and S. Bogliolo for assistance, S. Noselli and A. Hubstenberger for
390 comments on the manuscript, the PRISM Imaging facility (B. Monterroso and S. Ben-Aicha) and the
391 Microscopy Imaging Cytometry d'Azur (MICA) for microscopy support, the BIOINFO Bioinformatic
392 facility (A. Fortuné) for computational support, and M. Rigney for support with cryo-EM sample
393 preparation. Cryo-EM data were acquired at the UMass Chan Medical School Cryo-EM Core Facility.
394 This work was supported by the CNRS, INSERM, Université Côte d'Azur, ANR (ANR-19-CE13-0004-
395 01), EC (MSCA-ITN-2015-675407; MSCA-IF-2020-101029870; ERC-SyG-2020 951475) and FRM
396 (SPF202309017657) grants.

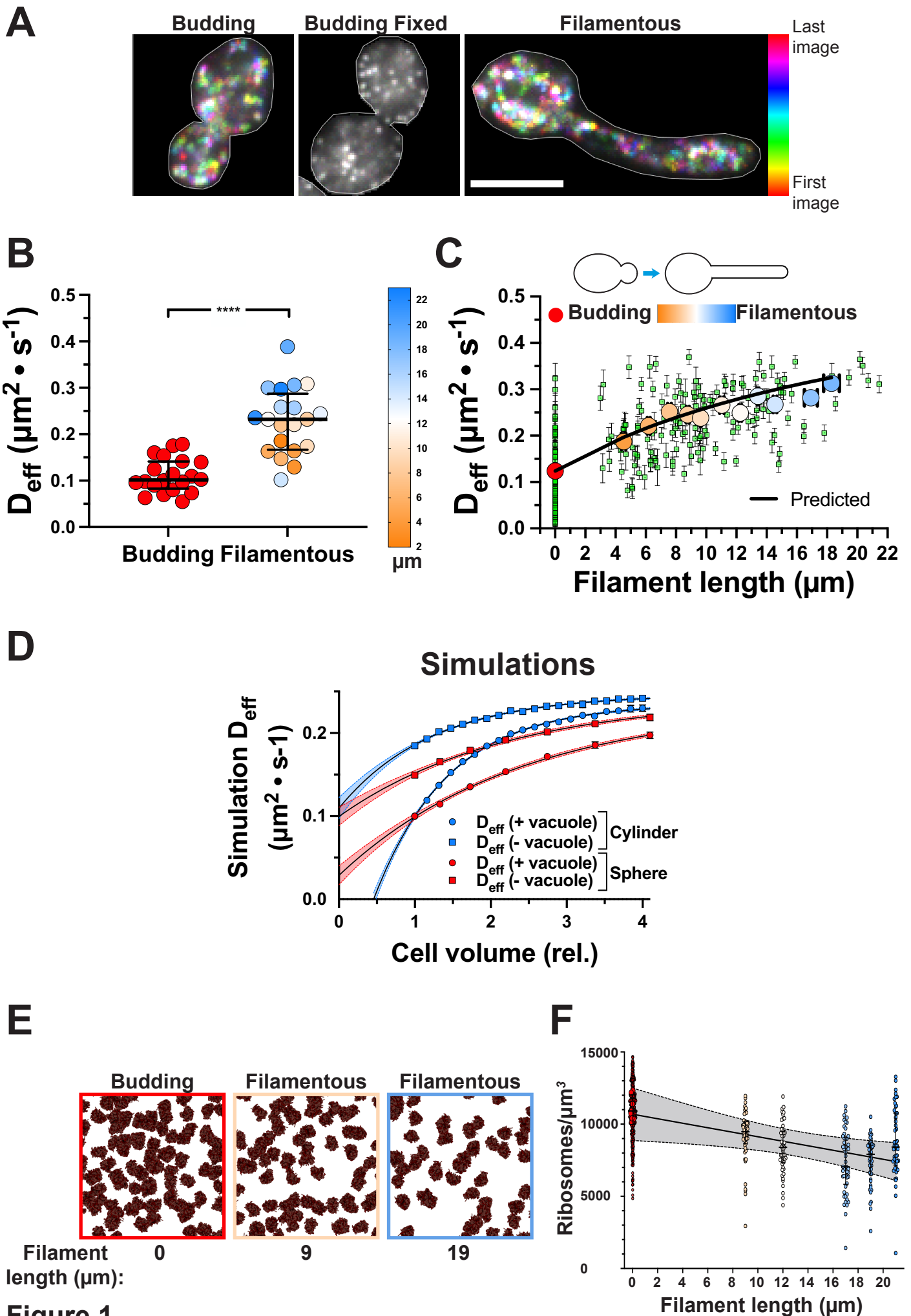


Figure 1

398 **Figure 1. Cytoplasmic fluidity increases with filament length.** A) Temporally color-coded projection
399 of GEM dynamics. Indicated cells were imaged, 250×10 msec. B) Dramatic increase in GEM D_{eff} in
400 filamentous cells. Filamentous growth was induced for 45-150 min. Each symbol is median cell D_{eff} (n
401 = 20 cells; 10-350 trajectories/cell). Mean filament length $12 \mu\text{m}$; color gradient indicates length with
402 **** < 0.0001 . C) Cytoplasmic fluidity increases with filament length. Filamentous growth induced on
403 agarose SC FBS, 45-125 min. Green squares are median cell D_{eff} and bars SEM. Values are grouped in
404 $2 \mu\text{m}$ filament length bins (red to blue gradient, with color indicating length as above; $n = 6 - 26$ cells;
405 1700 – 2600 trajectories). Red symbol is budding cells ($n = 67$; 2500 trajectories). The solid black line
406 is a fit using *eq 2* using overall cell volume; $r^2 = 0.95$. D) Simulation of GEM diffusion upon cell volume
407 increase. Particle D_{eff} in a cylindrical or spherical compartment, with ribosome crowders 20% at initial
408 cell volume (■, ■). Simulations with excluded compartments (*e.g.* vacuoles; ●, ●), further reduced
409 accessible volume from 80% (■, ■) to 20% (●, ●). Values are D_{eff} means (6000 particle simulations)
410 carried out 10 times. Data fit with an exponential plateau equation, $r^2 > 0.99$, 95% confidence levels. E)
411 Ribosome concentration is reduced in filamentous cells. Particle matching (cryo-EM 2DTM) of 60S
412 ribosomal subunits in indicated cells (filament length assessed by SEM). F) Ribosome density decreases
413 with filament length. Ribosomes concentration ($n = 8$ budding and 5 filamentous cells) determined by
414 cryo-EM 2DTM, small symbols values per ROI, large symbols median of each cell and symbol color
415 corresponds to filament length. Fit of medians to a straight line, $r^2 = 0.77$ with 95% confidence levels;
416 slope different from 0, $p < 0.0001$.
417

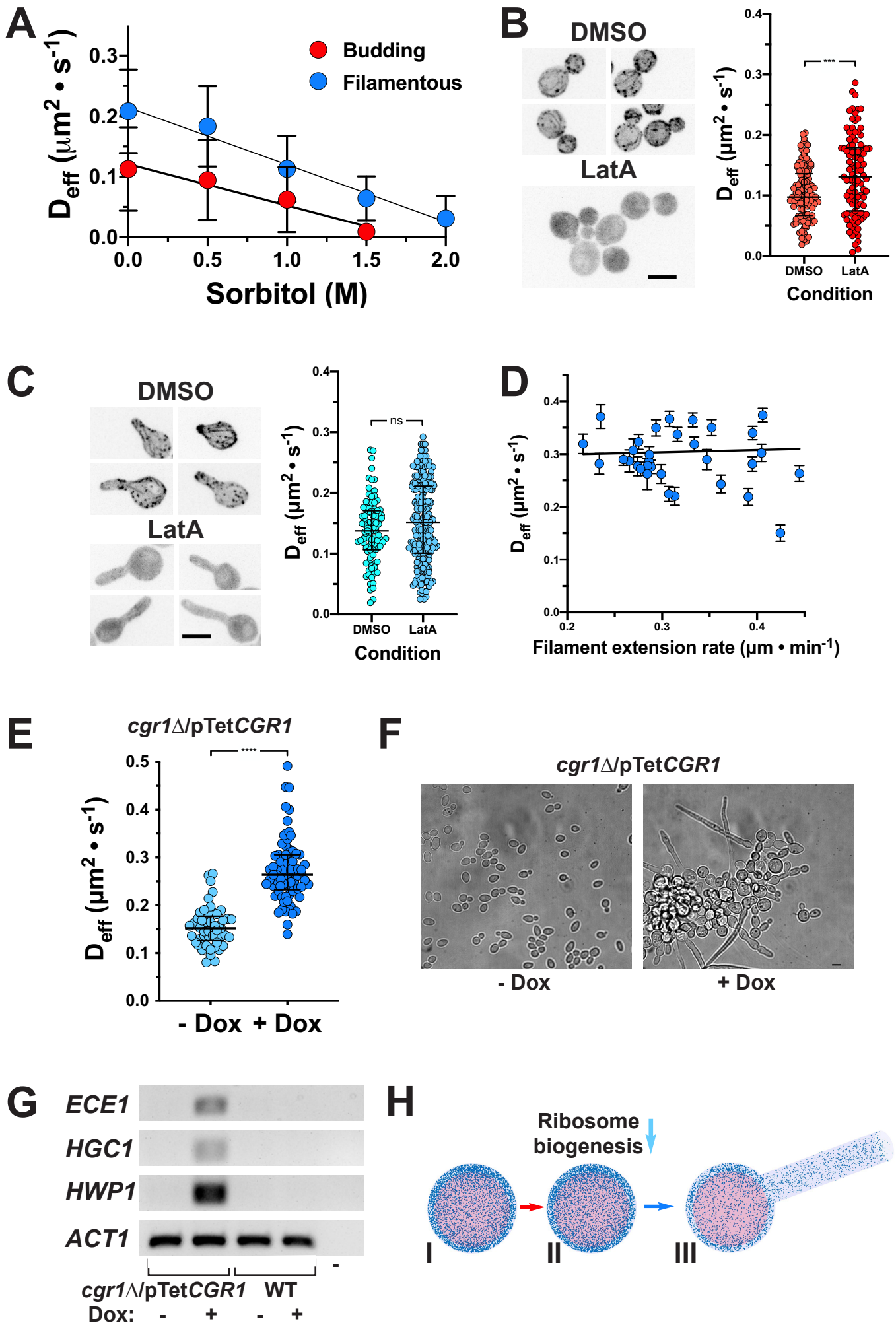


Figure 2

419 **Figure 2. Ribosome reduction increases cytoplasmic fluidity and results in filamentous growth.**
420 A) Cytoplasmic fluidity is higher in filamentous cells, at different sorbitol concentrations. Symbols are
421 the mean of 20-80 cells (11 - 200 trajectories/cell); bars are SD. Mean filament length was $7 \pm 3 \mu\text{m}$.
422 B) Disruption of actin cytoskeleton in budding cells increases cytoplasmic fluidity. Left: Max
423 projections of cells with LifeAct-RFP, with or without LatA. Right: symbol is median cell D_{eff} ($n \sim$
424 100; 10-180 trajectories/cell), *** = 0.0005. C) Disruption of actin cytoskeleton in filamentous cells
425 does not affect cytoplasmic fluidity. Left: Max projections of cells induced for 45 min with or without
426 LatA. Right: symbol is the median cell D_{eff} ($n = 100-200$; 15-150 trajectories/cell) of filamentous cells
427 with or without LatA, ns not significant. D) Cytoplasmic fluidity in filamentous cells is independent of
428 growth rate. Cells preincubated on agarose SC FBS, 40 min and followed for 60 min (images every 15-
429 20 min). Each symbol is the median cell D_{eff} with SEM and cell extension rate. Mean filament length
430 was $17 \pm 4 \mu\text{m}$. E) *CGR1* repression increases cytoplasmic fluidity. Each symbol is the median cell D_{eff}
431 ($n = 50-75$; 30-250 trajectories/cell); cells grown with or without Dox, **** < 0.0001 . F) *CGR1*
432 repression promotes filamentous growth. Representative cells with or without Dox. G) Hyphal-specific
433 genes are induced upon *CGR1* repression. *ECEL1*, *HGCI* and *HWPI* transcripts in indicated strains, with
434 or without Dox; *ACT1* as internal control. H) Schematic of ribosome biogenesis inhibition triggering to
435 filamentation. Red arrow indicates serum addition, which inhibits ribosome biogenesis (light blue
436 arrow), leading to ribosome dilution upon growth (dark blue arrow). Blue dots are ribosomes and pink
437 sphere vacuole compartment, inaccessible to ribosomes.

438 **References for Materials and Methods**

439

- 440 1 Delarue, M. *et al.* mTORC1 Controls Phase Separation and the Biophysical Properties of the
441 Cytoplasm by Tuning Crowding. *Cell* **174**, 338-349 e320 (2018).
442 [https://doi.org:10.1016/j.cell.2018.05.042](https://doi.org/10.1016/j.cell.2018.05.042)
- 443 2 Vernay, A., Schaub, S., Guillas, I., Bassilana, M. & Arkowitz, R. A. A steep phosphoinositide
444 bis-phosphate gradient forms during fungal filamentous growth. *J Cell Biol* **198**, 711-730
445 (2012). [https://doi.org:10.1083/jcb.201203099](https://doi.org/10.1083/jcb.201203099)
- 446 3 Zeng, G., Wang, Y. M. & Wang, Y. Cdc28-Cln3 phosphorylation of Sla1 regulates actin patch
447 dynamics in different modes of fungal growth. *Mol Biol Cell* **23**, 3485-3497 (2012).
448 [https://doi.org:10.1091/mbc.E12-03-0231](https://doi.org/10.1091/mbc.E12-03-0231)
- 449 4 Sbalzarini, I. F. & Koumoutsakos, P. Feature point tracking and trajectory analysis for video
450 imaging in cell biology. *Journal of Structural Biology* **151**, 182-195 (2005).
- 451 5 Lucas, B. A., Zhang, K., Loerch, S. & Grigorieff, N. *In situ* single particle classification reveals
452 distinct 60S maturation intermediates in cells. *Elife* **11** (2022).
453 [https://doi.org:10.7554/eLife.79272](https://doi.org/10.7554/eLife.79272)
- 454 6 Mastronarde, D. N. Automated electron microscope tomography using robust prediction of
455 specimen movements. *J Struct Biol* **152**, 36-51 (2005).
456 [https://doi.org:10.1016/j.jsb.2005.07.007](https://doi.org/10.1016/j.jsb.2005.07.007)
- 457 7 Ahlers, J. *et al.* apari: a multi-dimensional image viewer for Python (v0.4.18). *Zenodo* (2023).
458 [https://doi.org:https://doi.org/10.5281/zenodo.8115575](https://doi.org/https://doi.org/10.5281/zenodo.8115575)
- 459 8 Elferich, J., Schiroli, G., Scadden, D. T. & Grigorieff, N. Defocus Corrected Large Area Cryo-
460 EM (DeCo-LACE) for label-free detection of molecules across entire cell sections. *Elife* **11**
461 (2022). [https://doi.org:10.7554/eLife.80980](https://doi.org/10.7554/eLife.80980)
- 462 9 Grant, T., Rohou, A. & Grigorieff, N. cisTEM, user-friendly software for single-particle image
463 processing. *Elife* **7** (2018). [https://doi.org:10.7554/eLife.35383](https://doi.org/10.7554/eLife.35383)
- 464 10 Grant, T. & Grigorieff, N. Measuring the optimal exposure for single particle cryo-EM using a
465 2.6 Å reconstruction of rotavirus VP6. *Elife* **4**, e06980 (2015).
466 [https://doi.org:10.7554/eLife.06980](https://doi.org/10.7554/eLife.06980)
- 467 11 Elferich, J., Kong, L. & Grigorieff, N. CTFFIND5 provides improved insight into quality, tilt
468 and thickness of TEM samples. *Elife* (2024). [https://doi.org:10.7554/eLife.97227.1](https://doi.org/10.7554/eLife.97227.1)
- 469 12 Zgadzay, Y. *et al.* E-site drug specificity of the human pathogen *Candida albicans* ribosome.
470 *Sci Adv* **8**, eabn1062 (2022). [https://doi.org:10.1126/sciadv.abn1062](https://doi.org/10.1126/sciadv.abn1062)
- 471 13 Himes, B. & Grigorieff, N. Cryo-TEM simulations of amorphous radiation-sensitive samples
472 using multislice wave propagation. *IUCrJ* **8**, 943-953 (2021).
473 [https://doi.org:10.1107/S2052252521008538](https://doi.org/10.1107/S2052252521008538)
- 474 14 Lucas, B. A. *et al.* Locating macromolecular assemblies in cells by 2D template matching with
475 cisTEM. *Elife* **10** (2021). [https://doi.org:10.7554/eLife.68946](https://doi.org/10.7554/eLife.68946)
- 476 15 Ilker, E., Castellana, M. & Joanny, J. F. Long-time diffusion and energy transfer in polydisperse
477 mixtures of particles with different temperatures. *Phys Rev Res* **3** (2021).
478 [https://doi.org:10.1103/PhysRevResearch.3.023207](https://doi.org/10.1103/PhysRevResearch.3.023207)
- 479 16 Messner, C. B. *et al.* The proteomic landscape of genome-wide genetic perturbations. *Cell* **186**,
480 2018-2034 e2021 (2023). [https://doi.org:10.1016/j.cell.2023.03.026](https://doi.org/10.1016/j.cell.2023.03.026)
- 481 17 Wang, Z. *et al.* High-throughput proteomics of nanogram-scale samples with Zeno SWATH
482 MS. *Elife* **11** (2022). [https://doi.org:10.7554/eLife.83947](https://doi.org/10.7554/eLife.83947)
- 483 18 Demichev, V., Messner, C. B., Vernardis, S. I., Lilley, K. S. & Ralser, M. DIA-NN: neural
484 networks and interference correction enable deep proteome coverage in high throughput. *Nat*
485 *Methods* **17**, 41-44 (2020). [https://doi.org:10.1038/s41592-019-0638-x](https://doi.org/10.1038/s41592-019-0638-x)
- 486 19 Pedregosa, F. *et al.* Scikit-learn: Machine Learning in Python. *J Machine Learn Res* **12**, 2825-
487 2830 (2011).
- 488 20 Basante-Bedoya, M. A. *et al.* Two distinct lipid transporters together regulate invasive
489 filamentous growth in the human fungal pathogen *Candida albicans*. *PLoS Genet* **18**, e1010549
490 (2022). [https://doi.org:10.1371/journal.pgen.1010549](https://doi.org/10.1371/journal.pgen.1010549)

491 21 Wilson, R. B., Davis, D. & Mitchell, A. P. Rapid hypothesis testing with *Candida albicans*
492 through gene disruption with short homology regions. *J Bacteriol* **181**, 1868-1874 (1999).
493 <https://doi.org/10.1128/JB.181.6.1868-1874.1999>
494

495 **Supplementary Figure legends**

496

497 **Figure S1.** Projections of GEM trajectories. Representative budding and filamentous cells with
498 maximum projection of GEM images (A) and particle trajectories of GEMs (B) shown. False colored
499 LUT is indicated.

500

501 **Figure S2.** GEM effective diffusion is independent of its expression level. Each symbol represents the
502 median D_{eff} of indicated cells ($n = 25\text{-}35$ cells each condition; 25-120 trajectories per cell), expressing
503 GEMs under the control of either the *ADHI* or the *TEFI* promoter and grown at 30°C, with medians
504 and interquartile range indicated; ns, not significant.

505

506 **Figure S3.** Effective diffusion of all trajectories from budding and filamentous cells. Cells (20 each)
507 from Fig. 1B, with 900 – 3300 trajectories for each condition. Medians and interquartile range are
508 indicated; **** < 0.0001 .

509

510 **Figure S4.** GEM effective diffusion is somewhat reduced in filament compartment. A) GEM effective
511 diffusion in filament and mother cell compartments. Left panel: median D_{eff} of cells ($n = 74$) from Fig.
512 2C, in the absence of latrunculin A (LatA), with trajectories in whole cell, mother compartment and
513 filament compartment analyzed. Medians and interquartile range are indicated, with ** < 0.005 paired
514 t-test. Right panel: effective diffusion of all trajectories from filamentous cells from Fig. 2C in the
515 absence of LatA, with trajectories in whole cell ($n = 11100$), mother compartment ($n = 6300$) and
516 filament compartment ($n = 4700$) analyzed. Medians and interquartile range are indicated, with *** $<$
517 0.001 and * < 0.01 . B) GEM effective diffusion is similar in the mother and filament cell compartments
518 upon disruption of the actin cytoskeleton. Left panel: median D_{eff} of cells ($n = 74$) from Fig. 2C in the
519 presence of LatA, with all trajectories in whole cell, mother compartment and filament compartment
520 analyzed. Medians and interquartile range are indicated with ns, not significant paired t-test. Right
521 panel: effective diffusion of all trajectories from filamentous cells from Fig. 2C in the presence of LatA
522 with trajectories in whole cell ($n = 7300$), mother compartment ($n = 5000$) and filament compartment
523 analyzed ($n = 2100$). Medians and interquartile range are indicated with ns, not significant.

524

525 **Figure S5.** Simulation of GEM diffusion as a function of crowding. A) Representation of particle
526 diffusion simulation with ribosomes (blue dots) and vacuoles (large red spheres), within the cell
527 boundaries. B) Effect of cell geometry and excluded internal volume on particle diffusion. Ribosome
528 crowding was initially set to 20% of the cell compartment volume, either in the presence or absence of
529 vacuole compartment, which excluded an additional 60% of the cell. Note the surface to volume ratio
530 increases ~3-fold from a sphere to a cylinder of fungal cell size.

531

532 **Figure S6.** The GEM accessible volume increases significantly as the filament extends. The positions
533 of the GEMs and the outer edge of cells used in Fig. 1C was used to calculate the relative volume of
534 the whole cell (●) and the GEM accessible cytoplasm (●). The fraction of GEM accessible volume (●)
535 is the volume of the GEM accessible cytoplasm divided by the volume of the whole cell. Error bars
536 indicate standard deviation, data was fit either to a straight line ($r^2 = 0.72\text{-}0.76$) or one phase association
537 ($r^2 = 0.48$) for each condition with 95% confidence levels shown.

538

539 **Figure S7.** Theoretical equation for diffusion yields a good fit to the experimental data. Symbols
540 (circles, red to blue color indicating filament length) are data (filament length bins) from Fig. 1C and
541 grey squares/predicted line are from theoretical equation (eq 2), using GEM accessible volumes from
542 the results in Fig. S6. Correlation coefficient, $r^2 = 0.83$.

543

544 **Figure S8.** Relative abundance of ribosomal proteins decreases upon filamentation. Ribosomal proteins
545 levels were determined by Liquid-chromatography tandem mass spectrometry (LC-MS/MS) from
546 independent ($n = 4$) replicates, and normalized to the sample median protein levels. Control cells were
547 grown in YEPD at 30°C. In serum conditions, 50% FBS was added and samples were incubated at 37°C
548 for 0 and 90 min. Bars indicate means and ** < 0.01 .

549
550
551
552
553
554
555
556
557
558
559
560
561
562
563
564
565
566
567
568
569
570
571
572
573
574
575
576
577
578
579
580
581
582
583
584
585

Figure S9. 2D Template matching of 60S ribosomal subunits in cryo-EM images of budding cells. A) Montage of cryo-EM exposures of three representative cells. B) Manual segmentation of cytoplasmic regions. C) 2DTM detections of the 60S ribosomal subunit. D) Overlays of A-C. E) Histogram of 2DTM SNR of 60S ribosomal subunit detections.

Figure S10. 2D Template matching of 60S ribosomal subunits in cryo-EM images of filamentous cells. A) Images of three representative cells taken by the focused ion beam prior to milling. Length of filaments was measured using the image viewer of the AutoTEM software. B) Montage of cryo-EM exposures of representative cells. C) Manual segmentation of cytoplasmic regions. D) 2DTM detections of the 60S ribosomal subunit. E) Overlays of B-D. F) Histogram of 2DTM SNR of 60S ribosomal subunit detections.

Figure S11. GEM effective diffusion is reduced with increasing sorbitol concentrations. A) Increasing sorbitol concentration decreases GEM effective diffusion in budding cells. Median D_{eff} of cells ($n = 20-80$) from Fig. 2A, with 11 - 200 trajectories per cell (left), and effective diffusion of all trajectories from budding cells in Fig. 2A, with 600-4000 trajectories (right), as a function of sorbitol concentration. Medians and interquartile range are indicated. B) A higher concentration of sorbitol is required to fully abolish GEM dynamics in filamentous cells, compared to budding cells. Median D_{eff} of cells ($n = 20-80$) from Fig. 2A with 11 - 200 trajectories per cell (left), and effective diffusion of all trajectories from filamentous cells from Fig. 2A, with 600-4000 trajectories (right), as a function of sorbitol concentration. Medians and interquartile range are indicated.

Figure S12. The actin cytoskeleton restricts GEM diffusion in budding cells. Left panel: effective diffusion of all trajectories from budding cells in the presence and absence (DMSO) of LatA. Cells from Fig. 2B, with 5800-7200 trajectories for each condition. Medians and interquartile range are indicated; **** < 0.0001 . Right panel: effective diffusion of all trajectories from filamentous cells in the presence and absence of LatA. Cells from Fig. 2C, with 13600-21000 trajectories for each condition. Medians and interquartile range are indicated; **** < 0.0001 .

Figure S13. Repression of *CGRI* results in slow growth and reduction of rRNA levels. A) *CGRI* is fully repressed in doxycycline. The transcript level of *CGRI* was determined in *cgr1Δ/pTetCGRI* and wild-type strains, grown in the presence or absence of 5 $\mu\text{g/ml}$ Dox by RT-PCR with *ACT1* used as an internal control. B) Repression of *CGRI* results in slow growth. Indicated strains were incubated with or without 5 $\mu\text{g/ml}$ Dox on rich media containing agar for 2 days. C) Repression of *CGRI* results in a decrease in rRNA. Total RNA was isolated from the indicated strains.

586 Table S1. Strains used in this study.

Strain number	Relevant Genotype	Source
BWP17	<i>ura3Δ::λimm434/ura3Δ::λimm434 his1Δ::hisG/his1Δ::his arg4::hisG/arg4Δ::hisG</i>	21
PY173	Same as BWP17 with <i>ENO1/eno1::ENO1-tetR ScHAP4AD-3xHA-ADE2</i>	2
PY6413	Same as BWP17 with <i>adh1Δ::ADH1p-Pfv-GFP^{G206K}-ARG4</i>	This study
PY6414	Same as BWP17 with <i>adh1Δ::ADH1p-Pfv-GFP^{G206K}-CdHIS1</i>	This study
PY6523	Same as PY6413 with <i>tef1Δ::TEF1p-LifeAct-mScarlet-HIS1</i>	This study
PY6599	Same as BWP17 with <i>tef1Δ::TEF1p-Pfv-GFP^{G206K}-CdHIS1</i>	This study
PY7287	Same as PY173 with <i>CGRI/cgr1Δ::CdHIS1</i>	This study
PY7301	Same as PY7287 with <i>cgr1::URA3pTet_{off}CGRI</i>	This study
PY7322	Same as PY7287 with <i>adh1Δ::ADH1p-Pfv-GFP^{G206K}-ARG4</i>	This study

587

